

Signatures of the Seismic Source in EMD-Based Characterization of the 1994 Northridge, California, Earthquake Recordings

by Ray Ruichong Zhang, Shuo Ma, and Stephen Hartzell

Abstract In this article we use empirical mode decomposition (EMD) to characterize the 1994 Northridge, California, earthquake records and investigate the signatures carried over from the source rupture process. Comparison of the current study results with existing source inverse solutions that use traditional data processing suggests that the EMD-based characterization contains information that sheds light on aspects of the earthquake rupture process. We first summarize the fundamentals of the EMD and illustrate its features through the analysis of a hypothetical and a real record. Typically, the Northridge strong-motion records are decomposed into eight or nine intrinsic mode functions (IMF's), each of which emphasizes a different oscillation mode with different amplitude and frequency content. The first IMF has the highest-frequency content; frequency content decreases with an increase in IMF component. With the aid of a finite-fault inversion method, we then examine aspects of the source of the 1994 Northridge earthquake that are reflected in the second to fifth IMF components. This study shows that the second IMF is predominantly wave motion generated near the hypocenter, with high-frequency content that might be related to a large stress drop associated with the initiation of the earthquake. As one progresses from the second to the fifth IMF component, there is a general migration of the source region away from the hypocenter with associated longer-period signals as the rupture propagates. This study suggests that the different IMF components carry information on the earthquake rupture process that is expressed in their different frequency bands.

Introduction

Characterization of earthquake motion from observed records with the aid of proper data processing and analysis methods helps explain such seismological and geotechnical issues as source mechanism, directivity effects, and dynamic soil nonlinearity (Hall *et al.*, 1995; Heaton *et al.*, 1995; Somerville, 1997, 1998; Hartzell, 1998; and Hartzell *et al.*, 1999). These studies can also be used to quantify earthquake impact on various engineering systems and aid in seismic-resistant design and retrofit (Hall *et al.*, 1995; Heaton *et al.*, 1995; Somerville and Graves, 1996; Iwan, 1997; Somerville, 1998; Shinohara *et al.*, 1999; Sasani and Bertero, 2000; and Alavi and Krawinkler, 2000).

Huang *et al.* (1998a, 2001) have argued that conventional (e.g., Fourier-based) data processing and analysis techniques may yield distorted, indirect, or incomplete information about ground motion that is inherently nonstationary and is also likely the result of a nonlinear dynamic process. Because of its ability to faithfully characterize nonlinear (time-varying amplitude and frequency) and nonstationary data such as in earthquake recordings, empirical mode decomposition (EMD), developed by Huang *et al.*

(1998a, 1999) and used either individually or frequently together with Hilbert spectral analysis (HSA), can provide an alternative tool for earthquake data analysis and subsequent applications to seismology and earthquake engineering. In particular, based on the local characteristic timescale of any complicated time series, the EMD decomposes the data set into a finite, often small, number of intrinsic mode functions (IMFs) that admit a well-behaved Hilbert transform. The HSA of each IMF then defines instantaneous or time-dependent frequencies of the data that have physical meaning, unlike the HSA of the original data (Huang *et al.*, 1998a). The EMD, HSA, or their combination referred to as the Hilbert-Huang transform (HHT) typically help recover useful information from the data sets under investigation and subsequently improve understanding of the underlying physical process. Some recent applications of the approaches (e.g., EMD, HSA, and HHT) can be found in Huang *et al.* (1998a,b, 1999, 2001), Long (2001), Yang *et al.* (2000), Yang and Lei (2000), Loh *et al.* (2000, 2001), Loh (2000), Vincent *et al.* (2000), Zhang (2001a–c), Zhang and Larner (2002), and Zhang *et al.* (2003), ranging from solution of

classic nonlinear systems such as the Duffing equation to treatment of various observational data such as in bioengineering (e.g., blood-pressure variation), geophysics (e.g., ocean waves), engineering (e.g., system identification), among others.

In this study, we use the finite-fault inversion method to investigate a physical interpretation for EMD-based IMF components of the 1994 Northridge, California, earthquake recordings as they relate to source properties. Results will be compared with previously determined finite-fault source inversion solutions.

Fundamentals and Features of EMD

In this section, we present for completeness the fundamentals of EMD, which is summarized from Huang *et al.* (1998a, 1999). We then use a hypothetical time series and a real earthquake recording to demonstrate the features of EMD in analyzing nonlinear, nonstationary wave motion.

Empirical Mode Decomposition

The EMD builds on the assumption that any time series consists of different IMF components that are derived from the data. The IMF is defined by the following conditions:

1. Over the entire time series, the number of extrema (either maxima or minima) and the number of zero-crossings must be equal or differ at most by one; and
2. At any point, the mean value of the envelope defined by the local maxima and the envelope defined by the local minima is zero.

An IMF represents a simple oscillatory mode similar to a component in the Fourier-based simple harmonic function, but more general. One can decompose any waveform as follows: Identify all the local extrema. Connect all the local maxima by a cubic spline to produce the upper envelope, and repeat the procedure for the local minima to produce the lower envelope. The upper and lower envelopes should encompass all the data between them. Their mean can then be found as a function of time. The difference between the data and the mean should ideally be the first IMF component, which contains the finest scale or the shortest period component of the signal. Yet, in practice, all the conditions of an IMF cannot be achieved until the previous process, called the *sifting process*, is repeated. Specifically, the difference between the data and the mean after the first-round sifting process is treated as a new data set for the next-round sifting process if the difference does not satisfy all the conditions set in the definition of an IMF. This iterative sifting process typically runs a couple of times to single out the first true IMF component. One can then remove the first IMF component from the data to obtain the residue, which is treated as the new data and subjected to the same iterative sifting process as described previously. This procedure is repeated to obtain all the IMF components. The sifting process is ter-

minated if either the last IMF component or the residue is less than a predetermined value of consequence, or if the residue becomes a monotonic function from which no other IMF can be extracted. Mathematically, the data X can be represented by

$$X(t) = \sum_{j=1}^n c_j(t) + r(t) \quad (1)$$

where c_j is the j th IMF component, n is typically around 10 for most earthquake ground-motion records, and r is the residue.

The sifting process described previously may have a mode-mixing problem when the time series contain intermittency. *Intermittency*, here, refers to the phenomena in which two wave trains with significantly different amplitudes and frequencies occur intermittently. Examples of the two wave trains of this type are $A \sin(\omega_1 t_1 + \varphi_1)$ and $\varepsilon A \cos(\omega_2 t_2 + \varphi_2)$, where circular frequency ω_1 is significantly different from ω_2 , ε is a small factor, and more importantly, the range of t_2 is only a part of the range of t_1 . The former function might, for example, represent a dominant wave, while the latter might be one type of noise that occurs over only one or multiple portions of the dominant wave. Without any modification in the sifting process described above, the IMF components thus obtained might not be able to distinguish the two waves. This complication is called *mode mixing*, that is, wherever the small-amplitude wave is identified in one IMF or one intrinsic mode of oscillation, the underlying large-amplitude wave will also be partially included in the same IMF, and vice versa.

To solve the mode-mixing issue, a special operation, referred to as the *intermittency check*, is added in the EMD by specifying the frequency range in the sifting process. While the intermittency check in EMD can be used to prevent mode mixing in EMD and thus improve the interpretive value of each IMF component (e.g., Huang *et al.*, 1999; Yang and Lei, 2000), it also implies an intervention with a subjective condition in EMD. Such intervention could cause severe bias in the final IMF components (Huang *et al.*, 1999); thus, the intermittency check should be introduced only when the sifted results (IMF components) clearly show the problem of mode mixing. Intermittency check was not used in this study.

Features of EMD in Nonlinear, Nonstationary Data Processing

In this section, we use a hypothetical time series and a real earthquake record to demonstrate the characteristics of EMD in analyzing nonlinear and nonstationary wave motion. Figure 1 shows a hypothetical recording $y(t) = y_1(t) + y_2(t)$ that has nonlinear and nonstationary features consisting of decaying waves $y_1(t) = \cos[2\pi t + 0.5 \sin(2\pi t)]e^{-0.2t}$ having intrawave frequency $1 + 0.5\cos(2\pi t)$ in hertz and high-frequency harmonic noise $y_2(t) = 0.05 \sin(30\pi t)$. Note

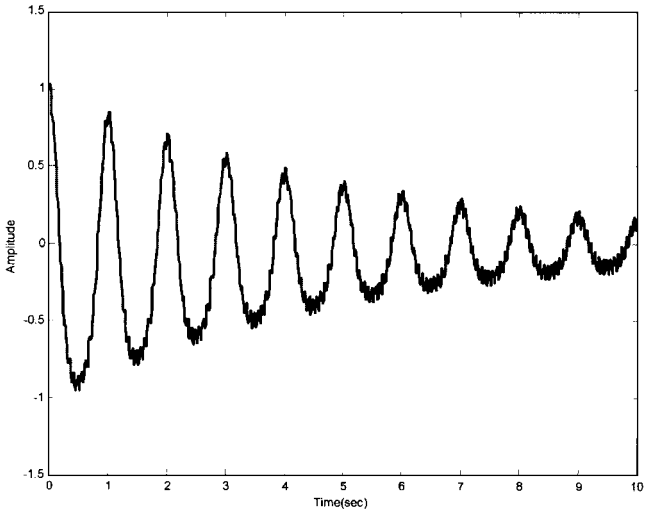


Figure 1. A hypothetical wave recording $y(t) = y_1(t) + y_2(t)$, consisting of waves $y_1(t) = \cos[2\pi t] + 0.5 \sin(2\pi t)e^{-0.2t}$ and high-frequency noises $y_2(t) = 0.05 \sin(30\pi t)$.

that the terminology “interwaves” and “intrawaves” was used by Huang *et al.* (1998a) for study in oceanography, indicating, respectively, waves with time-independent and time-dependent frequency. The waves have a nonsinusoidal waveform with sharp crests and rounded-off troughs, which are physically representative of one type of water wave. Figure 2 shows the five IMF components decomposed from the data by EMD. The first and second components (c_1 and c_2) in Figure 2 capture the noise and signal, respectively, while the other three (c_3 – c_5), with negligible amplitude, represent the numerical error in the EMD process. In comparison, the Fourier- and wavelet-based components may not have as clear a physical meaning as do the EMD-based ones (see Zhang *et al.* [2003], for detailed information). Although this is a trivial example, it serves to illustrate the utility of the EMD, which may not be as visually evident when considering earthquake recordings.

An earthquake recording contains more complicated information than does the hypothetical recording in Figure 1, as seen in Figure 3a,b, which shows, respectively, the acceleration record of the 1994 Northridge earthquake at station SCS1 and its Fourier amplitude spectrum. Figure 4a shows the nine IMF components decomposed from the data in Figure 3a by EMD, and Figure 4b shows their corresponding Fourier amplitude spectra. Typically, earthquake strong-motion data have only about 10 IMF components. As seen in Figure 4a,b, each component emphasizes a different oscillation mode with different amplitude and frequency content. The first IMF has the highest-frequency content. Frequency content decreases with increase in IMF component until the ninth IMF component, which is almost a linear function of time. The changing frequency content of the IMF components is similar to that in conventional Fourier-based bandpass filtering, but different in that the former does not

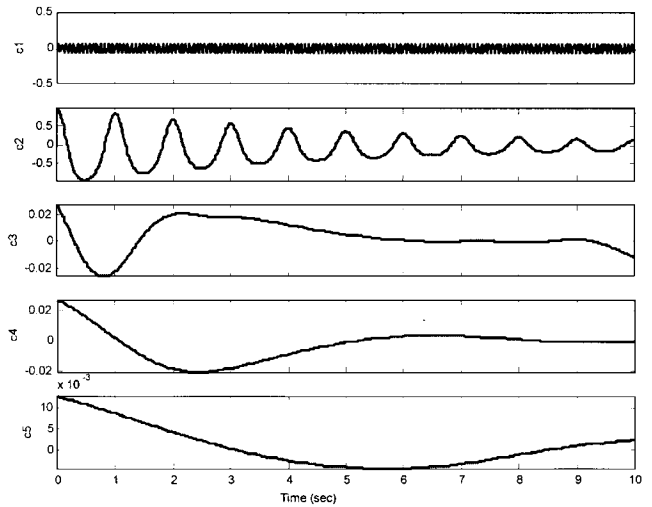


Figure 2. Five IMF components of the hypothetical wave recording in Figure 1.

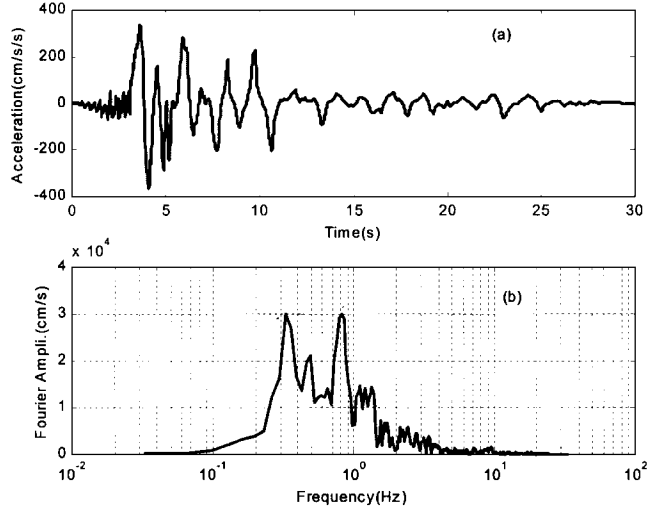


Figure 3. (a) Recorded ground motion at station SCS1 in the 1994 Northridge earthquake, (b) its Fourier spectrum.

have as clear a cutoff frequency as the latter (e.g., see the Fourier amplitude spectra of second and third IMF components in Fig. 4b). In addition, EMD is an automatic decomposition, compared with Fourier-based bandpass filtered components that are subjective as to the selection of frequency range. These IMF features, also shown in Huang *et al.* (1998a, 1999) and Zhang *et al.*, (2003), suggest that the EMD could reveal the oscillation mode of the underlying physical process that is different from the sinusoidal (and thus stationary) Fourier components in subjective bandpass filtered data and from mother-wavelet-dependent-wavelet components.

Since all the IMF components are extracted from acceleration records that are the result of seismic waves generated by the seismic source and propagating in the Earth, they

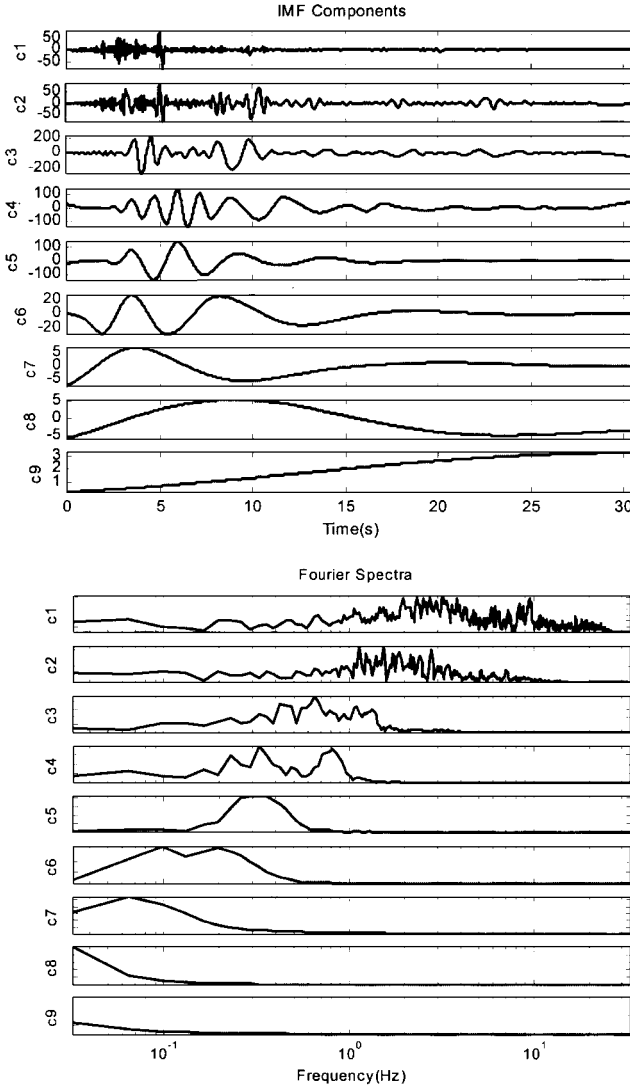


Figure 4. Nine IMF components of acceleration recording at station SCS1 (top) and their Fourier amplitude spectra (bottom).

should reflect the wave characteristics inherent to the rupture process and the earth medium properties. With this basis, we next use the 1994 Northridge, California, earthquake ground motion records to examine seismological signatures in the IMF components as they relate to source mechanisms. The primary reason for selecting the Northridge earthquake is that source models have been established using traditional data analysis such as Fourier-based bandpass filtering (Hartzell *et al.*, 1996; Wald *et al.*, 1996). The source model obtained from EMD data processing of the recordings will be compared with existing solutions, facilitating the physical interpretation of IMF components.

Source Inversion Investigation

To provide physical interpretations of IMF components as they relate to the source mechanism, we follow closely the source inversion study of the Northridge earthquake in

Hartzell *et al.* (1996). Specifically, the fault size used in this study is the same as in Hartzell *et al.* (1996). The fault has a strike of 122° and a dip of 40° to the southwest as seen in Figure 5. The fault plane measures 20 km in length and extends from a depth of 5–21 km for a down-dip width of 24.89 km. The fault is discretized into $14 \times 14 = 196$ subfaults (1.43×1.78 km), as seen in Figure 6. Each subfault has two slip weights (for rakes of 55° and 145°). We will, however, solve the inverse problem with the use of a modified finite-fault inversion method from the one used in Hartzell *et al.* (1996) and with the use of different data processing, which will be described in the two following sections.

Finite-Fault Inversion Method

Detailed mapping of spatial and temporal slip distributions of large-magnitude earthquakes is one of the principal goals of source inversion studies. After the 1979 Imperial Valley Earthquake, the finite-fault inversion method was developed to study the complexities of moderate to large-magnitude earthquakes (Olson and Apsel, 1982; Hartzell and Heaton, 1983). In the early work of Hartzell and Heaton (1983), the rupture propagation velocity was fixed or allowed to vary only slightly during the inversion. Attempts have been made to invert for both slip amplitude and rupture time (Beroza and Spudich, 1988; Hartzell, 1989; Hartzell and Iida, 1990). Recently, global inversion methods were introduced, where the slip amplitude, rupture time, and rise time were determined simultaneously (Hartzell *et al.*, 1996; Ji *et al.*, 2001). The following is a description of the method used in this study.

A finite fault is discretized into $n \times m$ subfaults, each of which is denoted by (j, k) or jk , corresponding to the j th along-strike and the k th down-dip subfault. Denote Green's functions G_{jk}^s and G_{jk}^d as the wave response at the ground surface (i.e., acceleration, velocity, or displacement) in a layered half-space due to unit slip on subfault jk in the strike (with superscript s in G) and down-dip (with superscript d in G) directions, respectively. The ground motion $u(t)$ caused by the finite fault can be synthesized as:

$$u(t) = \sum_{j=1}^n \sum_{k=1}^m D_{jk} [\cos(\lambda_{jk})G_{jk}^s(t) + \sin(\lambda_{jk})G_{jk}^d(t)] * \dot{S}_{jk}(t), \quad (2)$$

where D_{jk} and λ_{jk} are the dislocation amplitude and rake angle, respectively. $S_{jk}(t)$ is the rise-time function of the dislocation, which we assume is the same for all the subfaults; the dot over the head of $S_{jk}(t)$ stands for differentiation with respect to time t ; and the asterisk denotes convolution. Note that in calculating the Green's function, the time delay to the initiation of the earthquake at the hypocenter is considered, which is equal to the shortest on-fault distance from the hypocenter divided by the average rupture velocity.

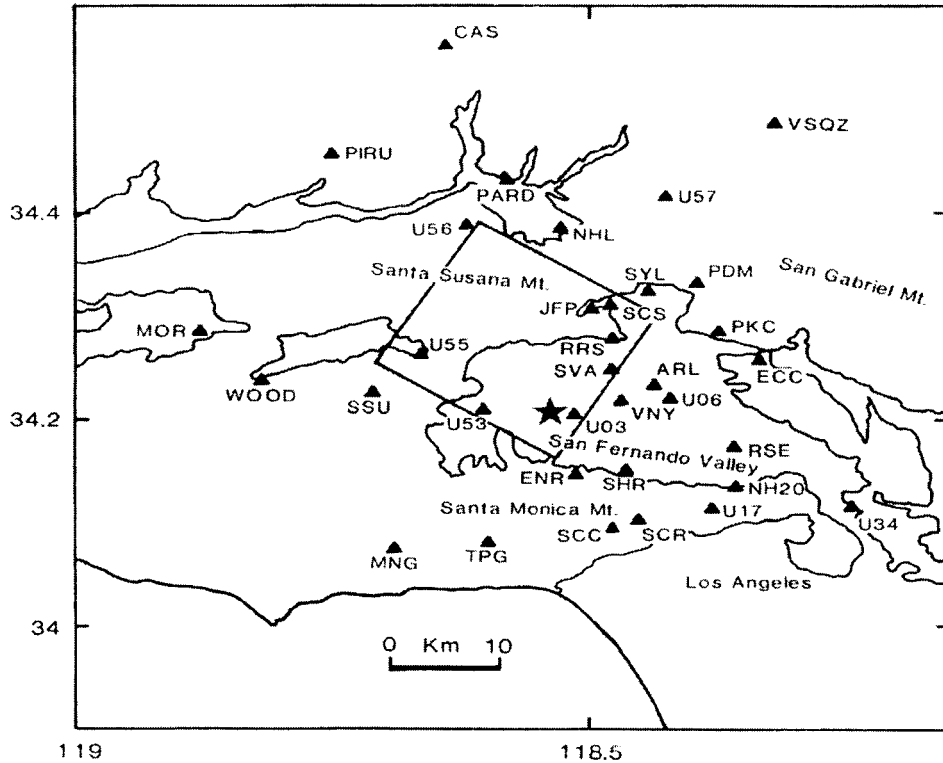


Figure 5. Map of strong-motion stations (solid triangles) used in the inversion for slip, rupture time, and rise time. The surface projection of the model fault plane is indicated by the heavy box. The mainshock epicenter is given by the star (from Hartzell *et al.*, 1996).

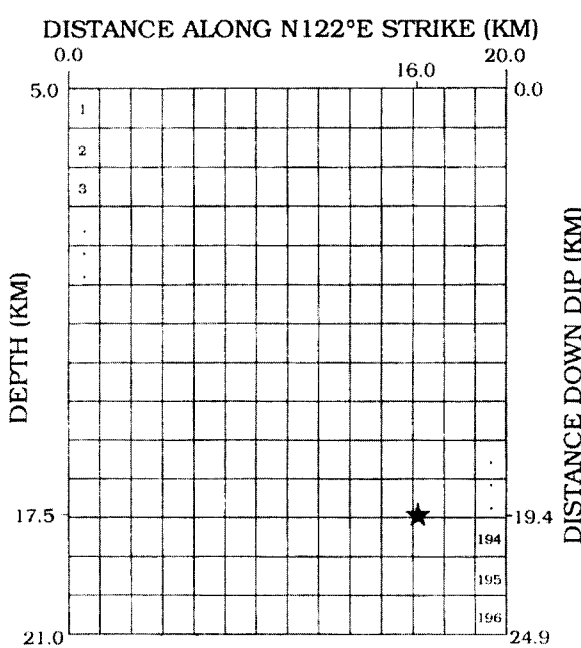


Figure 6. Parameterization of the fault plane. The hypocenter (34.211° N, 118.546° W, 17.5 km depth) is indicated by a star.

The observed records and the synthetics form an over-determined system of linear equations:

$$\mathbf{Ax} \approx \mathbf{b}, \quad (3)$$

where \mathbf{A} is the matrix of synthetics, \mathbf{b} is the observed data vector, and \mathbf{x} is the solution vector of the subfault dislocation weights. Each column of \mathbf{A} is composed of the synthetics, strung end to end, for a particular subfault and a particular mechanism (either strike-slip or dip-slip) for all the stations in the inversion. Similarly, \mathbf{b} is formed by stringing all the observation records end to end. Thus each time point on each record is explicitly included in the inversion. The number of columns of \mathbf{A} depends on the number of elements in x . The elements of \mathbf{x} are the amounts of strike-slip and dip-slip dislocations to be applied to each subfault to fit the observations. This equation can be solved by linear least squares, but the solution is unstable. The instability arises because \mathbf{A} is an ill-conditioned matrix, meaning that a small change in the data results in a large change in the solution. The problem can be stabilized by appending linear constraints giving

$$\begin{pmatrix} C_d^{-1} \mathbf{A} \\ \lambda_1 \mathbf{S} \\ \lambda_2 \mathbf{M} \end{pmatrix} \mathbf{x} \approx \begin{pmatrix} C_d^{-1} \mathbf{b} \\ 0 \\ 0 \end{pmatrix}, \quad (4)$$

where \mathbf{S} is a matrix of smoothing constraints in which the difference between the slips on adjacent subfaults is set equal to zero; \mathbf{M} is a matrix of minimization constraints where the slip on each subfault is set equal to zero; λ_1 and λ_2 are linear weights, whose magnitudes control the trade-off between satisfying the constraints and fitting the data. C_d is an *a priori* data covariance matrix. The data covariance matrix is diagonal and normalizes each data record to have peak amplitude of 1.0. Thus each record has more nearly an equal weight in the inversion. The solution vector \mathbf{x} is obtained by a Householder reduction method that involves a positivity constraint on the solution (Lawson and Hanson, 1974). Householder transformations avoid taking the product $\mathbf{A}^T \mathbf{A}$, which leads to a squaring of the singular values of the matrix and a loss of accuracy. Because full wave theory synthetics are used, the \mathbf{A} matrix is not sparse, and sparse matrix techniques cannot be used. The nonnegative constraint is imposed not only because negative slip on the fault is physically undesirable, but also because negative slips lead to destructive interference between subfaults and an unstable solution.

Processing of Observed Data

Instead of using a set of 35, two-horizontal-component ground velocity recordings for the inversion database as in Hartzell *et al.* (1996), this study uses IMF components of the same 70 acceleration records (Table 1 and Fig. 5). In particular, ground acceleration recordings are first corrected for the response of the instrument and then decomposed into IMF components. Typically, each record is decomposed into eight or nine IMF components, with the dominant frequency band of the same order IMF components similar for all the records (e.g., Fig. 4a,b).

This study uses four IMF components (i.e., c2–c5) for investigation since the first, highest-frequency IMF component likely contains information that is not simply or easily related to the seismic source (e.g., wave scattering in the heterogeneous media), and all the other IMF components (i.e., c6–c9) have small amplitudes compared with the four components used. Specifically, all the second IMFs (i.e., c2) extracted from the 70 data records are used as the inversion database (i.e., matrix b in equation [3] or [4]). The same procedure is repeated for the third (c3), fourth (c4), and fifth (c5) IMFs for the corresponding source inversion solutions.

There are two issues with using IMF components that need to be discussed. The first one is the stability of the IMF components relative to reasonable changes in the parameters used to calculate them. The three most relevant parameters are the data time window, the time step of the data, and the maximum number of sifting operations. Our tests show that the IMF components are stable with respect to the choice of the data window and the time step as long as the windows are started and ended at times of low amplitude and time steps are used that do not alias high frequencies. These are both usual signal-processing procedures. We have noticed that significantly different IMF components can be obtained

if the maximum number of sifting operations is set too low. We feel our results are reasonably stable based on our value of 10 sifting operations. This value would need to be adjusted depending on the frequency content of the data.

The second issue deals with the fact that because EMD is not based on a prescribed basis function, there is no complete correspondence between intrinsic modes of the same order from different time series. Also, in our study we must compare data and synthetics over a common frequency band. As shown in Figure 4b, each IMF component has a complicated Fourier spectrum with long tails to high and low frequencies. Comparing the spectra of all the IMF components at all 35 stations, however, we are able to identify frequency bands for each of the IMF components that contain most of the energy. These frequency bands are as follows: 1–5 Hz for c2, 0.5–2.5 Hz for c3, 0.3–1.5 Hz for c4, and 0.2–1 Hz for c5. The IMF components are then bandpass filtered with the respective frequency bands and resampled at a time step of 0.05 sec. Thus, although we do not have a rigorous mathematical justification for comparing IMF components across different stations, we do have an observation-based similarity between these components.

It should be noted here that the approach of bandpass filtering the time history of IMF with respective to its dominant frequency might be alternatively done by using EMD with an intermittency check. Intermittency check would allow for a general specification of the frequency band over which the IMF components are calculated. Because we did not observe clear mode mixture in the IMF components of the earthquake recordings, we did not use the intermittency criterion in EMD for extracting IMFs. In addition, an exponential, time-domain taper is used on each IMF component to remove nondirect, scattered energy later than about 7 sec after the first S-wave arrival. The IMF components of acceleration are used here as the observation data, which is the major difference from a typical finite-fault inversion.

Other Aspects of Source Inversion

The synthetics $u(t)$, the acceleration response of a layered half-space to the finite fault, are calculated using the discrete-wavenumber/finite-element method of Olson *et al.* (1984). We use two different velocity models (Table 2), one for rock sites and the other with slower surface velocities for soil sites, which are the same as in Hartzell *et al.* (1996). Synthetics are calculated for the frequency band 0–5 Hz and then bandpass filtered in the same manner as the IMF components using the respective frequency bands. The EMD is not used on the synthetics for two reasons. First, no linearity condition exists between IMF components of different records, so that linear combinations of IMF components of synthetic records do not equal the corresponding IMF component of the sum of the synthetics. Second, it is our objective to investigate the possible physical significance of IMF components, and to this end, we treat the IMF components as the observed ground-motion records.

The response of each subfault is obtained by summing

Table 1
Strong-Motion Stations Used in the Inversion

Station	Location	Latitude; ($^{\circ}$ N)	Longitude; ($^{\circ}$ W)	Owner*	Rock/Soil
ARL	Arleta, Nordhoff Avenue fire station	34.236	118.439	CDMD	Soil
CAS	Castaic, Old Ridge Route	34.564	118.642	CDNG	Rock
ECC	Energy Control Center	34.259	118.336	LADWP	rock
ENR	Encino, Encino Reservoir Dam	34.149	118.515	LADWP	Rock
JFP	Jensen Filtration Plant, administration building	34.312	118.496	USGS	Soil
MNG	Monte Nido, fire station	34.078	118.693	USGS	Rock
MOR	Moorpark	34.288	118.881	CDMG	Soil
NHL	Newhall, Los Angeles County Fire Department	34.387	118.530	CDMG	Soil
NH20	North Hollywood, 20-story hotel	34.138	118.539	CDMG	Soil
PARD	Santa Clarita, Pardee substation	34.435	118.582	SCE	Soil
PDM	Pacoima Dam, downstream	34.334	118.396	CDMG	Rock
PIRU	Lake Piru, Santa Felicia Dam	34.460	118.753	CDMG	Rock
PKC	Pacoima, Kagel Canyon fire station	34.288	118.375	CDMG	Rock
RRS	Sylmar, Rinaldi Receiving Station	34.281	118.479	LADWP	Soil
RSE	San Ferando, Receiving Station East	34.176	118.360	LADWP	Soil
SCC	Sepulveda Canyon	34.097	118.475	USGS	Rock
SCR	Stone Canyon, reservoir site	34.106	118.454	UCSB	Rock
SCS	Sylmar, converting station east	34.312	118.481	LADWP	Rock
SCS1	Sylmar, converting station west	34.311	118.490	LADWP	Soil
SHR	Sherman Oaks, 13-story commercial building	34.154	118.465	CDMG	Soil
SSU	Santa Susana, Department of Energy ground site	34.231	118.713	UCGS	Rock
SVA	Sepulveda, Veterans Administration hospital	34.249	118.175	USGS	Soil
SYL	Sylmar, county hospital parking lot	34.326	118.444	CDMG	Soil
TPG	Topanga, fire station	34.084	118.599	USGS	Rock
U03	Northridge, 17645 Saticoy	34.209	118.517	USC	Soil
U06	Sun Valley, 13248 Roscoe	34.221	118.421	USC	Soil
U17	Los Angeles, 8510 Wonderland	34.114	118.380	USC	Soil
U34	Los Angeles, 3036 Fletcher	34.115	118.244	USC	Soil
U53	Canoga Park, 7769 Topanga Canyon	34.212	118.605	USC	Rock
U55	Simi Valley, 6334 Katherine	34.264	118.666	USC	Soil
U56	Newhall, 26835 W. Pico Canyon	34.391	118.622	USC	Rock
U57	Canyon Country, 16628 W. Lost Canyon	34.419	118.426	USC	Soil
VNY	Van Nuys, 7-story hotel	34.221	118.471	CDMG	Soil
VSQZ	Vasquez Rocks Park	34.490	118.320	CDMG	Rock
WOOD	Wood Ranch Dam	34.240	118.820	CDMG	Rock

*CDMG, California Division of Mines and Geology; LADWP, Los Angeles Department of Water and Power; SCE, Southern California Edison; UCSB, University of California at Santa Barbara; USC, University of Southern California; USGS, U.S. Geological Survey.

Table 2
Velocity Structures

V_p (km/sec)	V_s (km/sec)	Density (g/cm 3)	Thickness (km)
<i>Rock Site</i>			
1.9	1.0	2.1	0.5
4.0	2.0	2.4	1.0
4.7	2.7	2.6	2.5
6.3	3.6	2.8	23.0
6.8	3.9	2.9	13.0
7.8	4.5	3.3	—
<i>Soil Site</i>			
0.8	0.3	1.7	0.1
1.2	0.5	1.8	0.2
1.9	1.0	2.1	0.2
4.0	2.0	2.4	1.0
4.7	2.7	2.6	2.5
6.3	3.6	2.8	23.0
6.8	3.9	2.9	13.0
7.8	4.5	3.3	—

point source synthetics, 48 for each subfault. Each point source response is lagged according to the rupture velocity and the travel time to the respective strong-motion stations to simulate a propagating rupture. The hypocenter is given by the local network determination of 34.211° N, 118.546° W, at a depth of 17.5 km (Wald *et al.*, 1996). Many of the strong motion records do not have trigger time information. For these stations the synthetic shear wave from the hypocenter is aligned with the first impulsive *S* wave in the original acceleration record.

The rupture velocity is fixed at 2.8 km/sec, and each subfault is allowed to slip within 3 separate time windows. The first-time window initiates at the arrival of the rupture front and the following two time windows are delayed by 0.4 sec and 0.8 sec, respectively. The source time function for each time window is a triangle with 0.6-sec duration (e.g., Fig. 7a) for the third, fourth, and fifth IMF components. The source time function for the second IMF component is a Brune function, $t e^{-\gamma t}$, where t is time and $\gamma = 10$ (Fig.

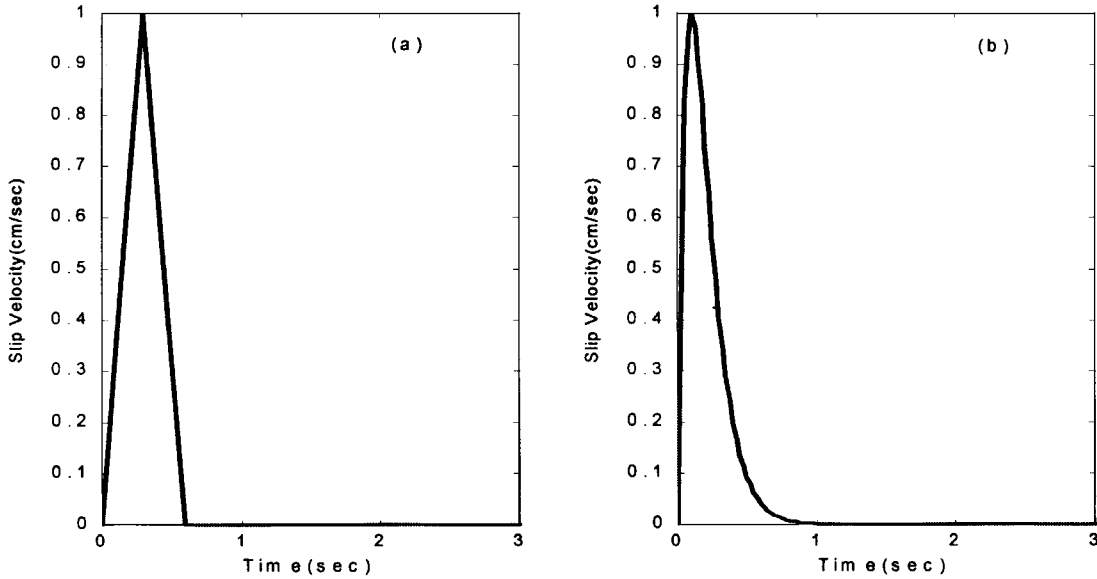


Figure 7. Plots of (a) triangle source-time function and (b) brune source-time function with $\gamma = 10$.

7b). The reason for making this selection of source time function for the second IMF is because the source time function plays an important role as a low-pass filter on the ground-motion synthetics and the second IMF component contains a relatively large proportion of high frequencies (up to 5 Hz). The use of the same triangle source function for the second IMF component filters out too many high frequencies to fit the records. Either time function would work as well and give similar results for the third, fourth, and fifth IMF components because of their lower frequency content. The rake of each subfault is determined by the vector sum of the slip weights obtained by the inversion for the two model values of 55° and 145° . Thus the rake may vary between these two bounds, and each subfault has a total of six model parameters (two slip values in each of three time windows).

Inversion Results

Figure 8a-d shows the spatial distributions of slip amplitude over the finite fault plane, for the second through fifth IMF components. The corresponding seismic moments are 2.5×10^{26} dyne cm, 2.15×10^{26} dyne cm, 1.37×10^{26} dyne cm, and 0.94×10^{26} dyne cm, respectively. Moment estimates from other studies range from 1 to 1.5×10^{26} dyne cm (Hartzell *et al.*, 1996; Wald *et al.*, 1996). The trend toward higher moment estimates with higher-frequency IMF component can be related to the assumed velocity structure in Table 2. The minimum shear-wave velocity at soil sites is 300 m/sec. This value was set for computational convenience. Boreholes in the Los Angeles area show near-surface velocities closer to 200 m/sec (Gibbs *et al.*, 1999). For a 20-m cap of 200 m/sec sediments, an amplification factor of about 1.4 between 3 and 5 Hz is obtained, that decreases to

approximately 1 at 0.5 Hz. Because of the high frequencies of the lower-order IMF components, these differences in velocities become important. The moment of each IMF component inversion is then generally consistent with the total moment of the earthquake. This result is in line with the fact that each inversion represents a different bandpass filtering of the same strong-motion data set.

Figure 9a-d shows plots of the waveform fits between synthetics and IMF components. While the waveform match at each station is generally acceptable, we notice that there are a couple of poor matches at some stations for the second and fifth IMF components in Figure 9a and 9d, respectively. In particular, the synthetics are larger than the observed second IMF component at stations JFP, NHL, SCS1, PARD, and U56 in Figure 9a. At the low-frequency end corresponding to the fifth IMF in Figure 9d, there is an over-prediction of amplitudes and a lower dominant frequency content in the IMF components at stations JFP, U55, MOR, and NHL. Some of these misfits can be attributed to soil nonlinearity, which is explained subsequently.

From laboratory experiments of soils under cyclic loads, it is generally recognized that the stress-strain relationship is nonlinear and hysteretic for strains larger than about 10^{-4} . Such soil nonlinearity corresponds primarily to a reduction of shear modulus and increased damping compared with linear soil (Hardin and Drnevich, 1972a,b; Erdik, 1987; Vucetic and Dobry, 1991; Beresnev and Wen, 1996; Field *et al.*, 1997; Beresnev *et al.*, 1998; Yu *et al.*, 1992). With a reduction of shear modulus for nonlinear soil in the top layer, the shear-wave velocity (v) also reduces. So does the resonant frequency ($v/4h$) of the top layer that is calculated from the two-way, zero-offset shear-wave travel time through the layer with thickness h . Ground-motion recordings in a non-

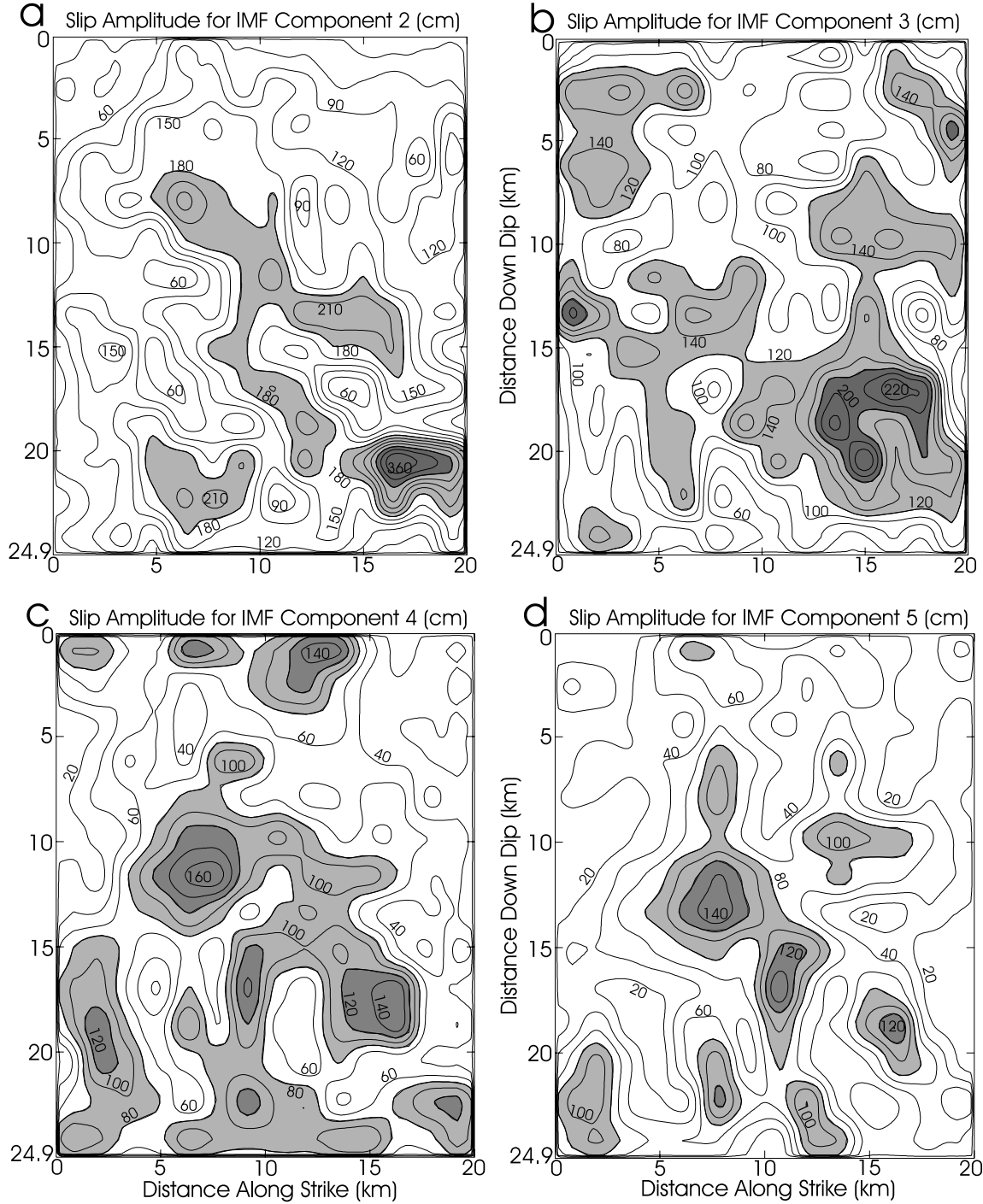


Figure 8. Contour plots of slip amplitudes in centimeters over the fault, corresponding, respectively, to the second to fifth IMF components of recordings; (a), left above; (b), right above; (c), left below; and (d), right below.

linear soft-soil layer could, therefore, show strong resonance at lower frequencies than for the linear case. For the problem at hand, the resonant frequency of the top soil layer in our model is 0.75 Hz, which is in the dominant frequency range of the fifth IMF component (0.2–1 Hz). The lower frequencies of the fifth IMF components at stations JFP, U55, MOR,

and NHL compared with the synthetics could be due to this effect. Field *et al.* (1998), Hartzell *et al.* (1998), and Frankel *et al.* (2002) report similar frequency shifts for the Northridge and Nisqually strong-motion data sets.

In addition, increased damping for nonlinear soil will decrease amplitudes, primarily at higher frequencies. In par-

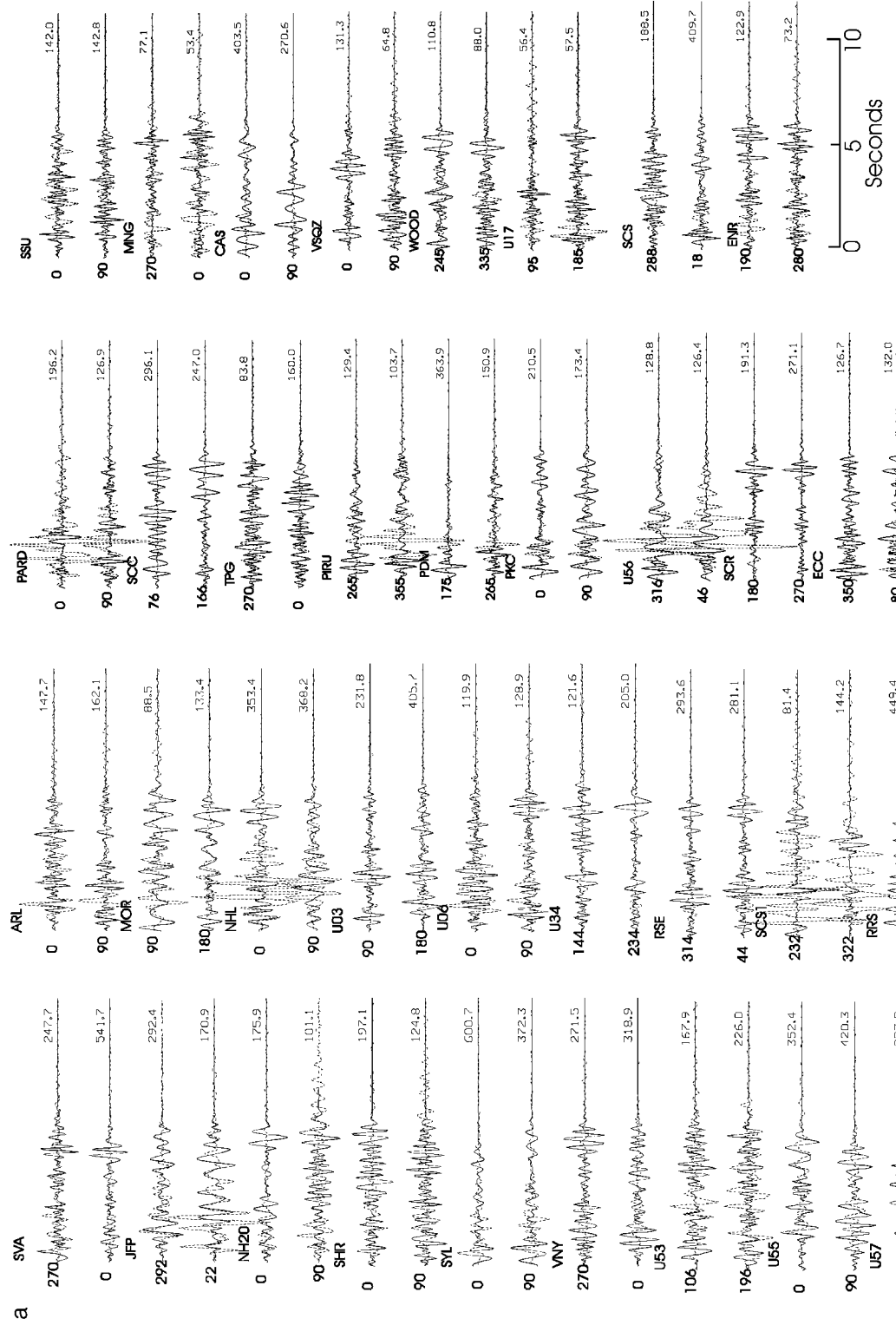


Figure 9. (a) Comparisons of IMF component c2 (solid lines) with the synthetics (dashed lines) for the least-square inversion. Data and synthetics are plotted on the same vertical scales. Peak amplitudes of the data record in cm/sec/sec are given for each trace.

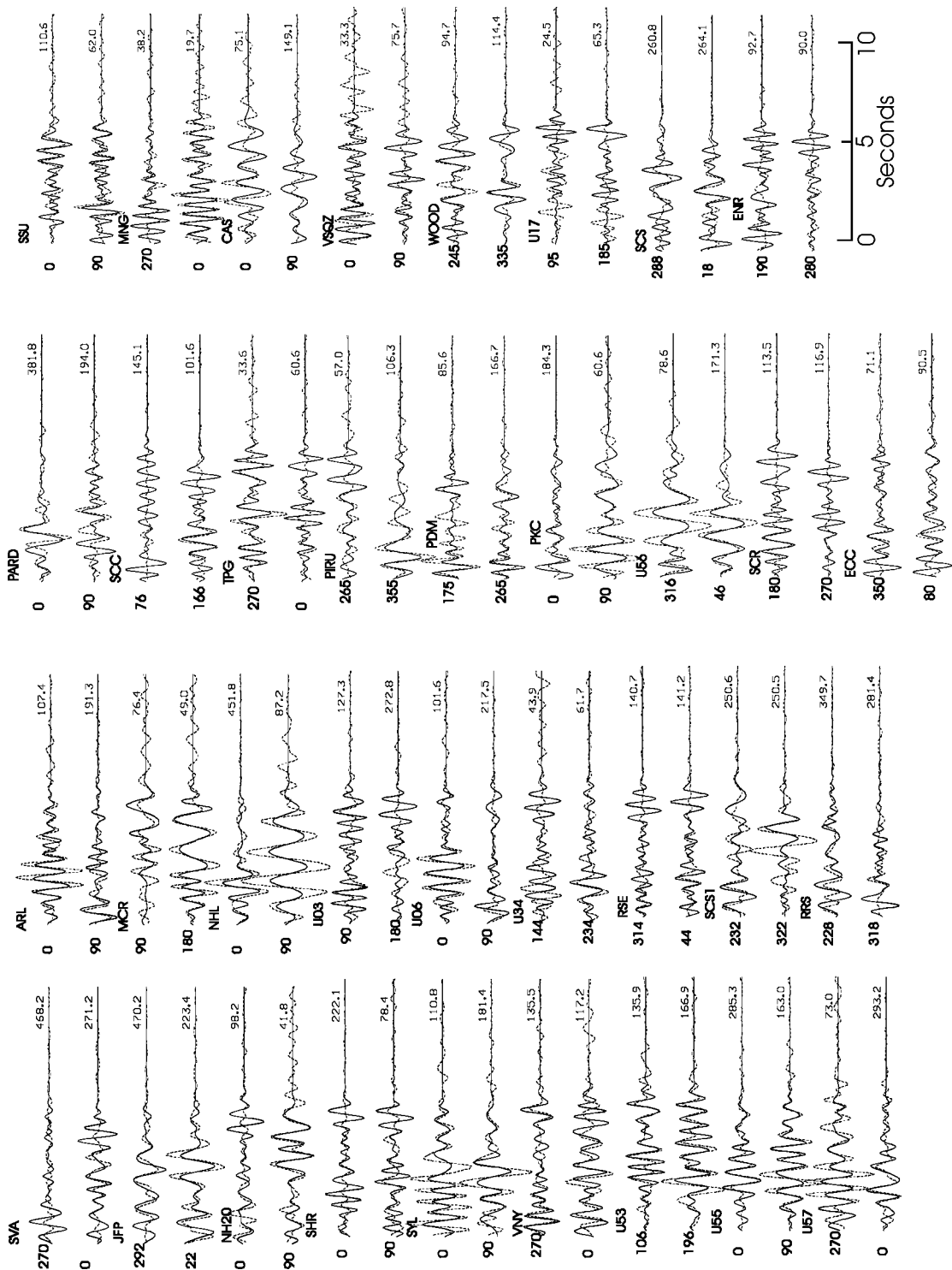


Figure 9. (continued) (b) Comparisons of IMF component c3 (solid lines) with the synthetics (dashed lines) for the least-square inversion. Data and synthetics are plotted on the same vertical scales. Peak amplitudes of the data record in cm/sec/sec are given for each trace.

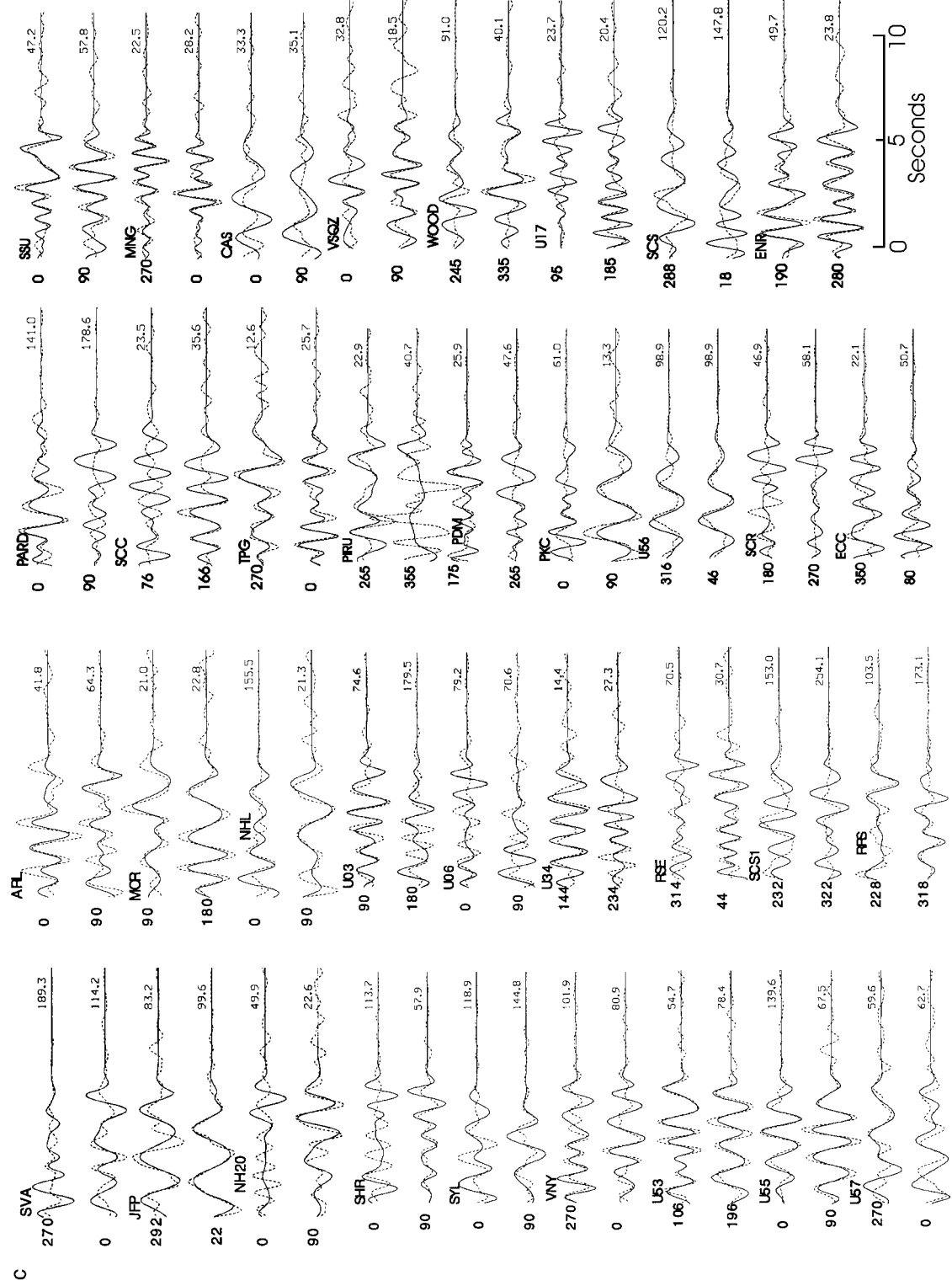


Figure 9. (continued) (c) Comparisons of IMF component c4 (solid lines) with the synthetics (dashed lines) for the least-square inversion. Data and synthetics are plotted on the same vertical scales. Peak amplitudes of the data record in cm/sec/sec are given for each trace.

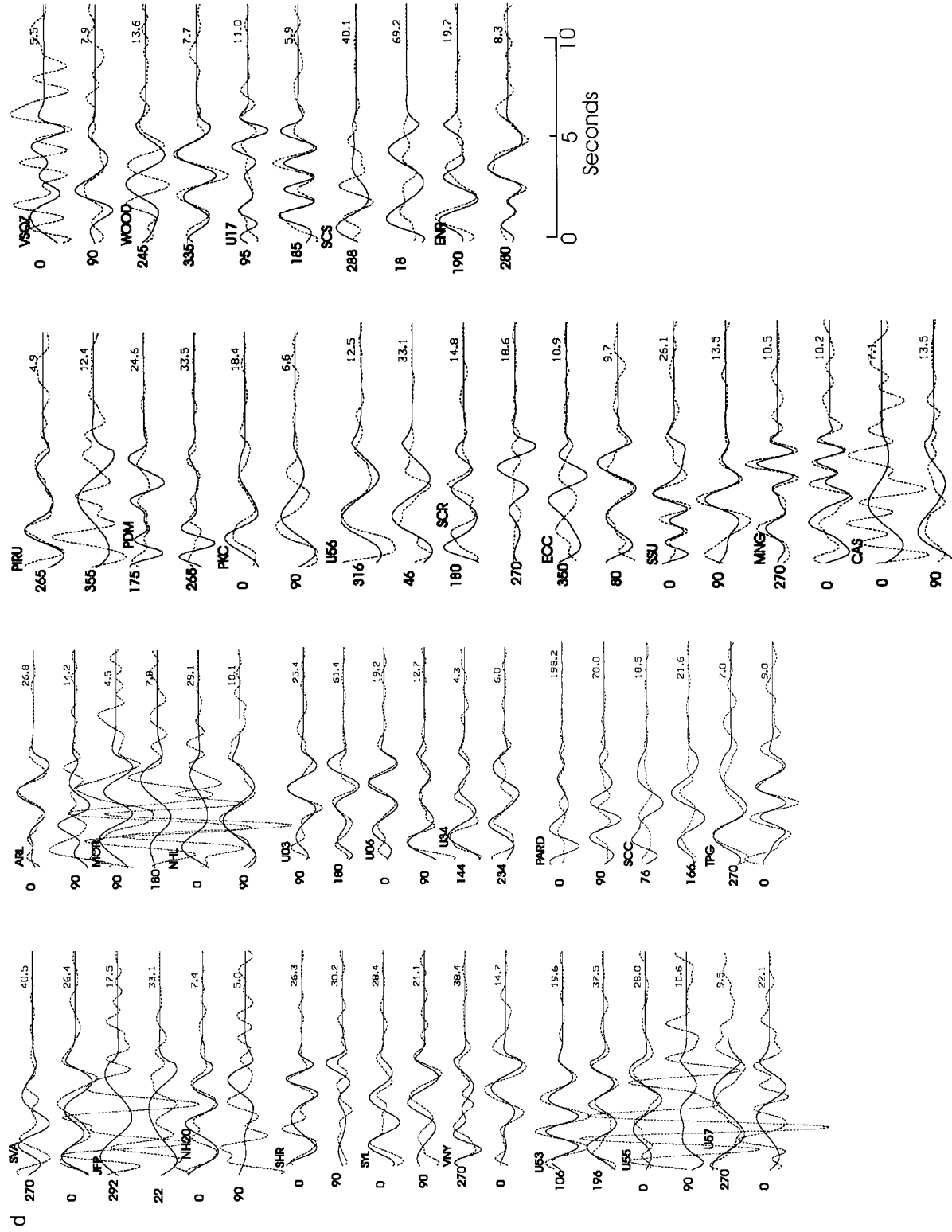


Figure 9. (continued) (d) Comparisons of IMF component c5 (solid lines) with the synthetics (dashed lines) for the least-square inversion. Data and synthetics are plotted on the same vertical scales. Peak amplitudes of the data record in cm/sec/sec are given for each trace.

ticular, several of the stations with amplitude mismatches between synthetics and the second IMF components were found to exhibit significant soil nonlinearity during the Northridge earthquake (Hartzell, 1998). The mismatch could, therefore, be due to a reduction in amplitude of high frequencies by the nonlinear soils. This explanation is subject to further investigations.

Signature of Seismic Source in IMF Components

To aid in the interpretation of the signature of the seismic source in IMF components of ground motion, we use as references the source-inversion solutions of the Northridge earthquake from Hartzell *et al.* (1996) and Wald *et al.* (1996), which are summarized as follows.

Inversion Solution of Hartzell *et al.* (1996)

Hartzell *et al.* (1996) used a hybrid search algorithm to solve the nonlinear problem of calculating slip amplitude, rake, rise time, and rupture time on a finite fault for the Northridge earthquake. For the observed data, acceleration records are first corrected for the response of the instrument and then integrated to give velocity, band pass filtered from 0.1 to 1 Hz, and re-sampled at a time increment of 0.1 sec. For the synthesized data, the velocity response of a layered half-space is calculated using the discrete-wavenumber/finite-element method of Olson *et al.* (1984), and then band-pass filtered from 0.1 to 1 Hz. With this approach, the low-frequency spatial distributions of slip amplitude, rake, rupture fronts, and rise time are found for the fault plane as shown in Figure 10a-d. Similarly, the corresponding high-frequency spatial distribution of slip was also found using a related approach and the envelopes of the acceleration records, which can be seen in Hartzell *et al.* (1996).

Basically, four regions of larger-amplitude slip are identified in Figure 10a: one at the hypocenter near a depth of 17 km (S1) with the largest slip amplitude, a second west of the hypocenter at about the same depth (S3), a third updip from the hypocenter at a depth of 10 km (S2), and a fourth updip from the hypocenter and to the northwest (S4). Figure 10d, together with Figure 10a and 10c, show that the slip near the hypocenter (S1) has a short rise time of about 0.5 sec, which increases to 1 sec for S3 and S2 and 1.5 sec for S4, as the major slip areas and rupture fronts move away from the hypocentral region. These results imply that slip region S1 generates higher-frequency waves, S2 and S3 generate moderate-frequency waves, and S4 generates lower-frequency waves.

Inversion Solution of Wald *et al.* (1996)

Wald *et al.* (1996) calculated a rupture model for the Northridge earthquake based on a joint inversion of near-source ground motion recordings, P and SH teleseismic body waves, Global Positioning System (GPS) displacement vectors, and permanent uplift measured along leveling lines. Figure 11a-d shows the slip distributions based on the in-

dividual data sets as well as the combined data set solution. The primary features of the model are summarized as follows. Three subevent locations (large-slip areas) are found: the first one is near the hypocenter; the second one with the largest slip amplitude is 12 km northwest and updip from the hypocenter and extends from the first one, and the third one is located about 8 km west of the hypocenter. The rupture pattern in Figure 11d is smoother than that in Figure 10a, because the former is influenced greatly by the geodetic inversion solution to GPS data in Figure 11c. In addition, the first and second subevent locations in Fig. 11d are similar to the locations of S1 and S4 in Figure 10a.

Interpretation of EMD-Based Inversion Solution

Comparing Figure 8a-d with Figure 10a-d and 11a-d, we observe the following:

1. The large slip amplitude region in Figure 8a, for the second IMF component, is essentially the first large slip amplitude region near the hypocenter, S1, in Fig. 10a and the first subevent in Figure 11d. As indicated in the “Inversion Solution of Hartzell *et al.* (1996)” section, S1 has the shortest rise-time (Fig. 10a,d) and thus generates the highest frequency waves among the four regions (S1, S2, S3, and S4). The second IMF component also has the highest frequency content among the four IMF components we used (Fig. 4b). Therefore, the second IMF component is likely predominantly the wave motion generated by the source near the hypocenter, with high-frequency content that might be related to a large stress drop with the initiation of the earthquake.
2. The largest slip region at the hypocenter in Figure 8a is nearly encircled by the largest slip region in Figure 8b, implying that the rupture begins at the hypocenter and then spreads out and in the process is moderated toward low-frequency radiation. Following this line, we can see generally from Figure 8a-d that the largest slip regions progress to the northwest from the hypocenter with the IMF components changing from the second (c2) to the fifth (c5). Since the frequency content in c2-c5 is decreasing (Fig. 4b), these four figures indicate that seismic waves are generated sequentially from dominant short-period signals to mainly longer-period signals as the rupture propagates. We notice that the spreading pattern of largest slip regions in Figure 8b-d is not as simple as in Figure 8a,b. This complexity might be attributed to the heterogeneity of barrier strengths on the fault.
3. While the rupture patterns in Figure 8a, 8b explain the starting phase of rupture in Figures 10a,c,d and 11d, the qualitative similarity of the rupture pattern between Figures 8c,d and 11d suggests that the latter phase of the rupture process is dominated by the same low-frequency source that dominates the geodetic solution in Figure 11c,d. The geodetic solution in Figure 11c is broader and smoother than the strong-motion-based solution in Figure 11a, indicating that the former will generate lower fre-

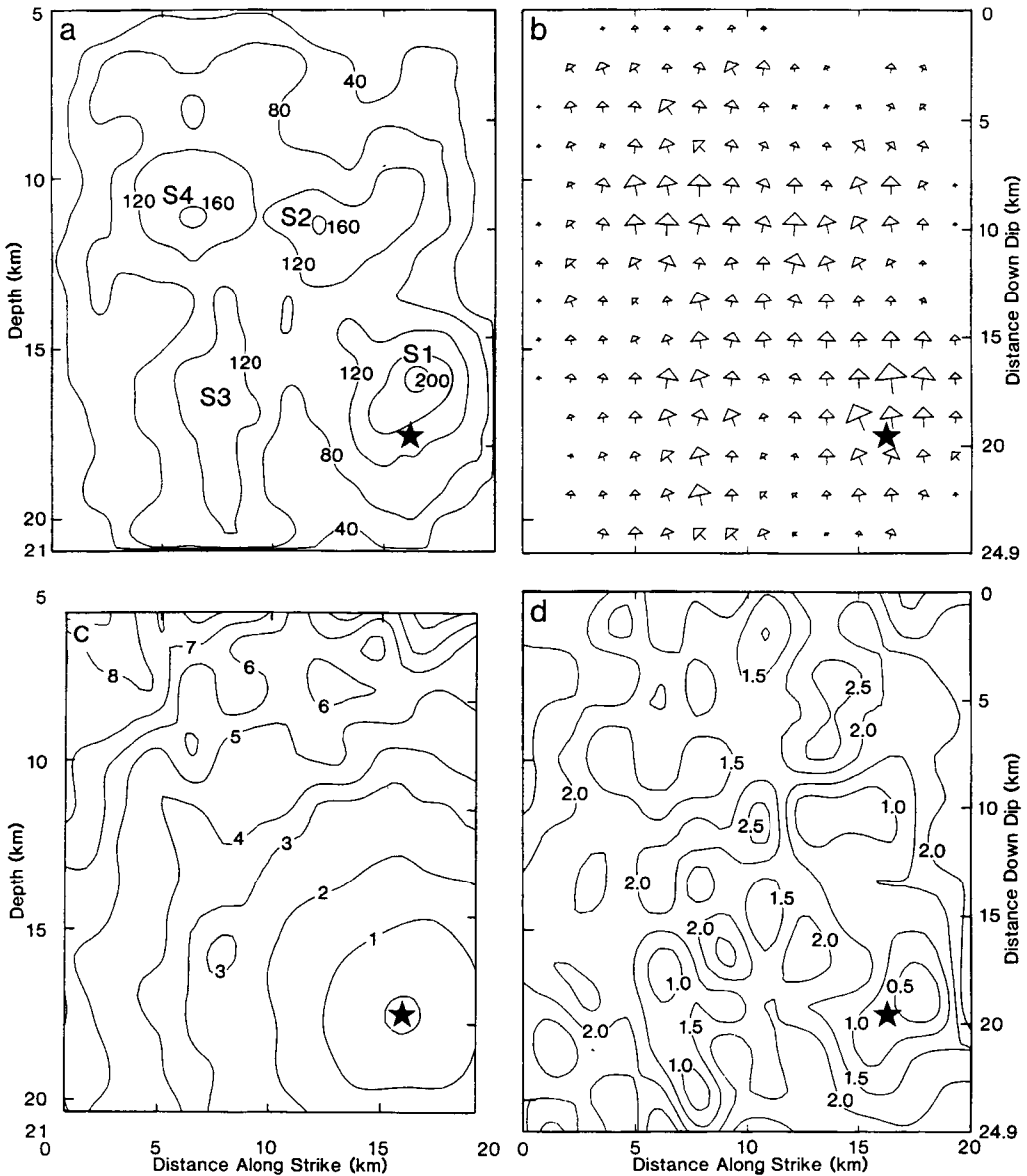


Figure 10. Plots of (a) slip amplitude (cm), (b) rake, (c) rupture fronts at 1-sec intervals, and (d) risetime at 0.5-sec contours for the preferred nonlinear, hybrid global search inversion (from Hartzell *et al.*, 1996).

quency motion than the latter. This result is consistent with the fact that the fourth and fifth IMFs, with source solutions in Figure 8c,d, contain seismic energy with lower dominant frequency band than the second and third IMFs, with source solutions in Figure 8a,b.

4. Other than the above largest slip regions, there are a few significant slip regions at the edges of the fault, which might be caused by the stopping of the rupture. As a partial validation, the larger slip region at the southwestern edge of the fault in Figure 8a is consistent with the high-frequency source-inversion solution of Hartzell *et al.* (1996).
5. Since each IMF component extracted from the strong-motion records is based on a different local characteristic

timescale of the recorded data, the seismic waves in the recording can be assessed from the observed timescales of the waves. These waves propagate and scatter through the earth media and constitute the complicated recorded ground motion at the stations with mixed timescale information. Since EMD can separate the mixed timescale information from a time series via IMF components, the whole rupture process should ideally be reconstructed. We should clarify here that this interpretation of IMF components is based on only the timescale of waves generated by the source. Actually, an earthquake recording results from both a rupture process at the source and wave propagation in the Earth, and thus is influenced by various scales of waves (spatial scales). Nevertheless, the cur-

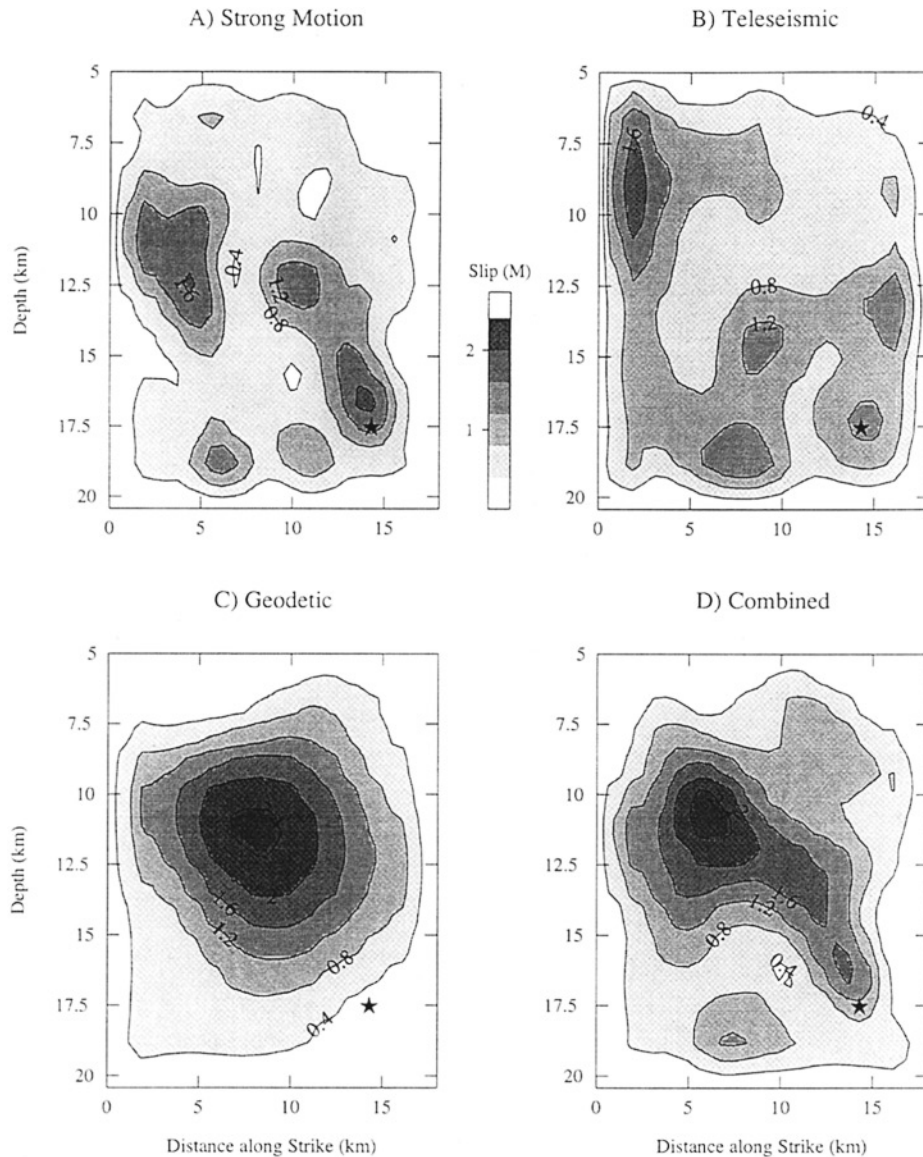


Figure 11. Comparison of the cross sections of the (a) strong-motion, (b) teleseismic, (c) geodetic, and (d) combined dislocation models. Contour interval is 0.4 m. View is from the southwest and perpendicular to (above) the fault plane. The scale bar shows the slip shading in 0.4-m increments (from Wald *et al.*, 1996).

rent study suggests that the IMF components can carry information on the seismic rupture process.

Concluding Remarks and Discussions

This study uses a finite-fault inverse method to examine the seismological significance of the EMD-based IMF components of the 1994 Northridge earthquake ground motion recordings as they relate to the seismic source mechanism. Comparison of the current study results with existing source inverse solutions that use traditional data processing suggests that the IMF components can contain information that shed light on aspects of the earthquake rupture process. We

must point out that such observations are, at this point, qualitative and suggestive, not quantitative and conclusive. Validation requires further examination of other ground-motion recordings. Nevertheless, work to date suggests the following observations:

1. The second IMF component of the Northridge strong motion is explained predominantly by a 5-km-wide source centered at the hypocenter. This high-frequency component may represent a localized high-stress drop source associated with the initiation of rupture. The third IMF component has a source region that nearly encircles the source region of the second component. The fourth and fifth components appear to extend this evolution with

- source regions further from the hypocenter and lower radiated frequencies. This trend is consistent with the results of Hartzell *et al.* (1996) that show longer rise times farther from the hypocenter.
2. The EMD explores temporal variation in the characteristic timescales of data. Therefore, it has the potential to recover useful information from the data on the underlying physical process having a local characteristic timescale as a sole or dominant feature, such as the hypothetical recording in this study, the solution of the Duffing equation, or observational data in oceanography (Huang *et al.*, 1998a, 1999). On the other hand, the EMD might recover only partial or mixed information in the IMF components if the underlying physical process has multiple scales or local characteristic timescales. Earthquake recordings might belong to the latter case, in which the IMF components contain information from the rupture process at the source, wave propagation, and scattering in the Earth. Therefore, it will be a subject of continuing study to understand the physical significance of IMF components of seismic recordings as they relate not only to source mechanisms, but also directivity, soil heterogeneity, soil nonlinearity, and their combination.
 3. Contrary to almost all the existing methods (such as Fourier and wavelet transformations with *a priori* harmonics and mother wavelet), the EMD is *a posteriori* and adaptive, based on the simple assumption that any time series consists of different simple IMF components, which are based on and derived from the data. On the one hand, the EMD does not have some merits possessed by Fourier and wavelet transformations. For example, Fourier (wavelet) components of a summation of two functions are equal to the summation of the Fourier (wavelet) components of each of the two functions, while the EMD components are not. Such a linearity feature implies that the Fourier or wavelet transformation is more readily adapted to source linear-inverse study than the EMD. On the other hand, because of the *a posteriori* and adaptive nature of EMD in data processing, the EMD might reveal certain types of information (such as with the nonlinear, nonstationary waves in Fig. 2) that the traditional methods (with *a priori* nature) might not be able to reveal effectively (Huang 1998a, 2001).

Acknowledgments

The authors would like to express their sincere gratitude to Dr. Norden E. Huang, Research Oceanographer in NASA Goddard Space Flight Center and the originator for the HHT method, for his invaluable introduction to HHT analysis, encouragement, and advice for this study. All the IMF components in this study were calculated using the Hilbert-Huang Transformation Toolbox, Professional Edition V1.0 (2000). This work was supported by the National Science Foundation with Grant No. 0085272 with Dr. R.J. Fragaszy as Program Director. The opinions, findings, and conclusions expressed herein are those of the authors and do not necessarily reflect the views of the sponsors. The article was significantly improved by comments from two anonymous reviewers.

References

- Alavi, B., and H. Krawinkler. (2000). Consideration of near-fault ground motion effects in seismic design, on CD-ROM, in *Proceedings of 12th World Conference on Earthquake Engineering*, Auckland, New Zealand, 4 February 2000.
- Beresnev, I. A., and K. L. Wen (1996). Nonlinear soil response—A reality, *Bull. Seism. Soc. Am.* **86**, 1964–1978.
- Beresnev, I. A., E. H. Field, P. A. Johnson, and K. E. A. Van Den Abeele (1998). Magnitude of nonlinear sediment response in Los Angeles basin during the 1994 Northridge, California, earthquake, *Bull. Seism. Soc. Am.* **88**, 1097–1084.
- Beroza, G. C., and P. Spudich (1988). Linearized inversion for fault rupture behavior: applications to the 1984 Morgen Hill, California, earthquake, *J. Geophys. Res.* **93**, 6275–6296.
- Erdik, M. (1987). Site response analysis, Strong Ground Motion Seismology, Erdik, M. and Toksoz, M., eds., D. Reidel Publishing Company, Dordrecht, 479–543.
- Field, E. H., P. A. Johnson, I. A. Beresnev, and Y. Zeng (1997). Nonlinear ground-motion amplification by sediments during the 1994 Northridge earthquake, *Nature* **390**, 599–602.
- Field, E. H., Y. Zeng, P. A. Johnson, and I. A. Beresnev (1998). Pervasive nonlinear sediment response during the 1994 Northridge earthquake: Observations and finite-source simulations, *J. Geophys. Res.* **103**, 26,869–26,883.
- Frankel, A. D., D. L. Carver, and R. A. Williams (2002). Nonlinear and linear site response and basin effects in Seattle for the M6.8 Nisqually, Washington, Earthquake, *Bull. Seism. Soc. Am.* **92**, 2090–2109.
- Gibbs, J. F., J. C. Tinsley, D. M. Boore, and W. B. Joyner (1999). Seismic velocities and geological conditions at twelve sites subjected to strong ground motion in the 1994 Northridge, California, earthquake: A revision of OFR 96-740, U.S. Geol. Sur. Open-File Rept. 99-446, 142 pp.
- Hardin, B. O., and V. P. Drnevich (1972a). Shear modulus and damping in soils: measurement and parameter effects, *J. Soil. Mech. Foundations Div. ASCE* **98**, 603–624.
- Hardin, B. O., and V. P. Drnevich (1972b). Shear modulus and damping in soils: design equation and curves measurement and parameter effects, *J. Soil. Mech. Foundations Div. ASCE* **98**, 667–692.
- Hall, J. F., Heaton, T. H., Halling, M. W., and D. J. Wald. (1995). Near-source ground motion and its effects on flexible buildings, *Earthquake Spectra* **11**, 569–605.
- Hartzell, S. (1989). Comparison of seismic waveform inversion results for the rupture history of a finite fault: applications to the 1986 North Palm Springs, California, earthquake, *J. Geophys. Res.* **94**, 7515–7534.
- Hartzell, S. (1998). Variability in nonlinear sediment response during the 1994 Northridge, California, earthquake, *Bull. Seism. Soc. Am.* **88**, 1426–1437.
- Hartzell, S., and T. Heaton. (1983). Inversion of strong ground motion and teleseismic waveform data for the fault rupture history of the 1979 Imperial Valley, California, earthquake, *Bull. Seism. Soc. Am.* **73**, 1553–1583.
- Hartzell, S., and Iida M. (1990). Source complexity of the 1987 Whittier Narrows, California, earthquake from the inversion of strong motion records, *J. Geophys. Res.* **95**, 12,475–12,485.
- Hartzell, S., S. Harmsen, A. Frankel, and S Larsen (1999). Calculation of broadband time histories of ground motion: Comparison of methods and validation using strong-ground motion from the 1994 Northridge earthquake, *Bull. Seism. Soc. Am.* **89**, 1484–1504.
- Hartzell, S., P. Liu, and C. Mendoza (1996). The 1994 Northridge, California, earthquake: Investigation of rupture velocity, risetime, and high-frequency radiation, *J. Geophys. Res.* **101**, 20,091–20,108.
- Heaton, T. H., J. F. Hall, D. J. Wald, and M. W. Halling (1995). Response of high-rise and base-isolated buildings to a hypothetical Mw 7.0 blind thrust earthquake, *Science* **267**, 206–211.

- Hilbert-Huang Transformation Toolbox (2000). Professional Edition V1.0. Princeton Satellite Systems, Inc., Princeton, N.J.
- Huang, N. E. (2001). Recent development on the HHT, informal lecture for the group who participated in the first invited session: The HHT Technique at work, in *5th World Multiconference on Systemics, Cybernetics and Informatics*, 22–25 July 2001, Orlando, Florida.
- Huang, N. E., C. C. Chern, K. Huang, L. W. Salvino, S. R. Long, and K. L. Fan (2001). A new spectral representation of earthquake data: Hilbert spectral analysis of station TCU129, Chi-Chi, Taiwan, 21 September 1999, *Bull. Seism. Soc. Am.* **91**, 1310–1338.
- Huang, N. E., Z. Shen, and R. S. Long (1999). A new view of nonlinear water waves—Hilbert Spectrum, *Ann. Rev. Fluid Mech.* **31**, 417–457.
- Huang, N. E., S. Zheng, S. R. Long, M. C. Wu, H. H. Shih, Q. Zheng, N.-C. Yen, C. C. Tung, and H. H. Liu (1998a). The Empirical Mode Decomposition And Hilbert Spectrum For Nonlinear And Nonstationary Time Series Analysis, *Proc. R. Soc Lond. A* **454**, 903–995.
- Huang, W., Z. Shen, N. E. Huang, and Y. C. Fung (1998b). Engineering analysis of biological variables: an example of blood pressure over 1 day, *Proc. Natl. Acad. Sci.* **4816**–4821.
- Iwan, W. (1997). Drift spectrum: Measure of demand for earthquake ground motions, *ASCE J. Eng. Mech.* **123**, 397–406.
- Ji, C., D. J. Wald, and D. V. Helmberger (2002). Source description of the 1999 Hector, California earthquake, part I: wavelet domain inversion theory and resolution analysis, *Bull. Seism. Soc. Am.* **92**, 1192–1207.
- Lawson C. L., and R. J. Hanson (1974). *Solving Least Squares Problems*. Prentice-Hall, Inc., Englewood Cliffs, New Jersey.
- Loh, C. H. (2000). Seismic response measurement and system identification of bridges, in *Proceedings of Workshop on Mitigation on Earthquake Disaster by Advanced Technologies*, Los Angeles, California, 2–3 March 2000.
- Loh, C. H., T. C. Wu, and N. E. Huang (2001). Application of the empirical mode decomposition-Hilbert spectrum method to identify near-fault ground-motion characteristics and structural responses, *Bull. Seism. Soc. Am.* **91**, 1339–1357.
- Loh, C. H., T. C. Wu, and N. E. Huang (2000). Application of EMD + HHT method to seismic response data of building structure, in *Proceedings of International Workshop on Annual Commemoration of Chi-Chi Earthquake*, C. H. Loh and W. I. Liao (Editors), Vol. II, 270–281.
- Long, S. (2001). *The HHT Technique at Work*, 5th World Multiconference on Systemics, Cybernetics and Informatics, 22–25 July 2001, Orlando, Florida, (CD-ROM).
- Olson, A. H., and Aspel, R. (1982). Finite fault and inversion theory with applications to the 1979 Imperial Valley earthquake, *Bull. Seism. Soc. Am.* **72**, 1969–2001.
- Olson, A. H., J. A. Orcutt, and G. A. Frazier (1984). The discrete wave-number/finite element method for synthetic seismograms, *Geophys. J. R. Astr. Soc.* **77**, 421–260.
- Sasani, M., and Bertero, V. V. (2000). Importance of severe pulse-type ground motions in performance-based engineering: historical and critical review, on CD-ROM, in *Proceedings of 12th World Conference on Earthquake Engineering*, Auckland, New Zealand, 4 February 2000.
- Shinozuka, M., G. Deodatis, R. Zhang, and A. S. Papageorgiou (1999). Modeling, synthetics and engineering applications of strong earthquake wave motion, *J. Soil Dyn. Earthquake Eng.* **18**, 209–228.
- Somerville, P. (1997). Engineering characteristics of near fault ground motion, *SMIP97 Seminar on Utilization of Strong-Motion Data*, 8 May 1997, Los Angeles, California.
- Somerville, P. (1998). Development of an improved representation of near-fault ground motions, *SMIP98 Seminar on Utilization of Strong Motion Data*, 15 September 1998, California Department of Conservation, Division of Mines and Geology, Oakland, California.
- Somerville, P. G., and Graves, R. W. (1996). Ground motions: site response and near-fault effects, in *Tall Building Structures—A World View*, 169–185.
- Vincent, H. T., S. L. J. Hu, and Z. Hou (2000). Damage detection using empirical mode decomposition method and a comparison with wavelet analysis, in *Structural Health Monitoring 2000*, F. K. Chang (Editor), Technomic Publishing Co., Lancaster, Pennsylvania, 891–900.
- Vucetic, M., and R. Dobry (1991). Effect of soil plasticity on cyclic response, *J. Geotech. Eng.* **117**, 89–107.
- Wald, D. J., T. H. Heaton, and K. W. Hudnut (1996). The slip history of the 1994 Northridge, California, earthquake determined from strong-motion, teleseismic, GPS, and leveling data, *Bull. Seism. Soc. Am.* **86**, S49–S70.
- Yang, J. N., and Y. Lei (2000). Identification of tall buildings using ambient noisy wind vibration data, *Advances in Structural Dynamics*, J. M. Ko and Y. L. Xu (Editors), Vol. II, Elsevier Science Ltd., Oxford, U.K., 1093–1100.
- Yang, J. N., P. K. Kagoo, and Y. Lei (2000). Parametric identification of tall buildings using ambient wind vibration data, in *8th ASCE Specialty Conference on Probabilistic Mechanics and Structural Reliability*, Notre Dame, Indiana, 24–26 July 2000, (CD-ROM).
- Yu, G., G. Anderson, and R. Siddharthan (1992). On the characteristics of nonlinear soil response, *Bull. Seism. Soc. Am.* **72**, 218–244.
- Zhang, R. (2001a). Features of HHT-based, low-frequency earthquake recordings, in *Proceedings of 8th International Conference on Structural Safety and Reliability*, R. B. Corotis, G. I. Schueller, and M. Shinozuka (Editors), 17–22 June 2001, Newport Beach, California.
- Zhang, R. (2001b). The signature of structural damage—an HHT view, in *Proceedings of 8th International Conference on Structural Safety and Reliability*, R. B. Corotis, G. I. Schueller, and M. Shinozuka (Editors), 17–22 June 2001, Newport Beach, California.
- Zhang, R., and K. Larner (2002). Rationale of HHT data processing for studies of seismology and earthquake engineering, *Proceedings of Turkey-Taiwan Earthquake*, NSF-Tubitak Grantee Workshop, 24–26 March 2002, Antalya, Turkey.
- Zhang, R., R. King, and L. Olson (2001c). An HHT-based structural damage diagnosis, *The First Asia-Pacific Workshop on Smart Materials*, Nanjing, China, 28–29 May 2001.
- Zhang, R., S. Ma, E. Safak, and S. Hartzell (2003). HHT analysis of dynamic and earthquake motion recordings, *ASCE J. Eng. Mech* (in press).

Division of Engineering
Colorado School of Mines
Golden, Colorado 80401
(R.R.Z.)

Department of Geological Sciences
University of California, Santa Barbara
Santa Barbara, California 93106
(S.M.)

U.S. Geological Survey
MS 966 Box 25046
Denver, Colorado 80225
(S.H.)

Manuscript received 15 November 2001.